MATERIALS SCIENCE

Anion ordering enables fast H^- conduction at low temperatures

Hiroki Ubukata[1], Fumitaka Takeiri[2,3], Kazuki Shitara[4], Cédric Tassel[1], Takashi Saito[5,6], Takashi Kamiyama[5], Thibault Broux[1], Akihide Kuwabara[7], Genki Kobayashi[2,3], Hiroshi Kageyama[1,8,9]*

The introduction of chemical disorder by substitutional chemistry into ionic conductors is the most commonly used strategy to stabilize high-symmetric phases while maintaining ionic conductivity at lower temperatures. In recent years, hydride materials have received much attention owing to their potential for new energy applications, but there remains room for development in ionic conductivity below 300°C. Here, we show that layered anion-ordered $Ba_{2-\delta}H_{3-2\delta}X$ (X = Cl, Br, and I) exhibit a remarkable conductivity, reaching 1 mS cm^{-1} at 200°C, with low activation barriers allowing H^- conduction even at room temperature. In contrast to structurally related BaH_2 (i.e., Ba_2H_4), the layered anion order in $Ba_{2-\delta}H_{3-2\delta}X$, along with Schottky defects, likely suppresses a structural transition, rather than the traditional chemical disorder, while retaining a highly symmetric hexagonal lattice. This discovery could open a new direction in electrochemical use of hydrogen in synthetic processes and energy devices.

INTRODUCTION

Solid-state materials with fast ionic conductivity find diverse applications such as batteries, sensors, and fuel cells. Reducing operating temperatures is an important issue, but some materials drastically lose their ionic conductivity by undergoing a structural phase transition to lower-symmetry structure upon cooling (*1*, *2*). The best-known strategy to circumvent this problem is the introduction of chemical disorder to stabilize a high-temperature (HT) phase. For example, in yttria-stabilized zirconia (YSZ), a Y^{3+}-for-Zr^{4+} substitution for the cubic ZrO_2 suppresses the transition to a tetragonal or monoclinic form and induces oxide ion conductivity (*1*). Likewise, the hexagonal HT phase of $Li(CB_9H_{10})$ can be stabilized by forming a solid solution with $Li(CB_{11}H_{12})$, which enables a fast lithium ion conductivity at room temperature (*3*). Other host materials that have successfully stabilized HT forms via chemical disorder include AgI (*1*), O^{2-} conductors [e.g., $Ba_2In_2O_5$ (*1*, *2*) and $La_2Mo_2O_9$ (*4*)], Li^+ conductors [e.g., $Li_7La_3Zr_2O_{12}$ (*5*) and $LiBH_4$ (*6*)], and Na^+ conductors [e.g., $Na_2B_{12}H_{12}$ (*7*) and $Na_4Zn(PO_4)_2$ (*8*)].

Hydride materials have raised recent interest due to the unique characteristics of H^- anions such as high lability, high polarizability, and high compressibility, which have opened up new synthesis routes (*9*, *10*) and lead to novel properties including catalysis (*11*, *12*). In view of the light mass of H^-, its monovalence, and the redox potential of H_2/H^- (−2.23 V versus standard hydrogen electrode), hydride ion conductivity appears promising as next-generation electrochemical energy storage systems with high voltage and high energy density (*13*, *14*). In 2015, BaH_2 with a hexagonal close packing (hcp) of Ba cations (Fig. 1A) was shown to achieve a H^- conductivity of 0.04 to 0.2 S cm^{-1} at 450° to 630°C, an order of magnitude higher than that of typical oxide ion conductors and proton conductors (e.g., YSZ and Nd-doped $BaCeO_3$) (*13*). However, its conductivity drops rapidly at 450°C when it undergoes a transition to an orthorhombic phase with a distorted hcp (Ba) lattice (fig. S1). Subsequent studies of H^- conduction have shifted to oxyhydrides including $Ln_{2-x-y}Sr_{x+y}LiH_{1-x+y}O_{3-y}$ (Ln = La, Pr, Nd) (*14*, *15*), Ba_2MHO_3 (M = Sc and Y) (*16*, *17*), and $LaH_{3-2x}O_x$ (*18*, *19*). Although the inclusion of oxide ions may improve thermal stability, high H^- conductivity over 10^{-3} S cm^{-1} is only reached above 300°C.

Hydride-based antiperovskites with a soft anion sublattice have recently shown promise as alkali ion conductors (*20*). The use of soft anions compared to oxide ions would also be beneficial for hydride conductivity. Thus, we aimed to investigate Ba_2H_3X hydride-halides (X = Cl, Br, and I) with the anti-Li_3LaSb_2 structure (space group: $P\bar{3}m1$) (*21*, *22*), which consists of alternating stacking of face-sharing HBa_6 and XBa_6 octahedral layers along the hexagonal c axis, with additional hydride anions in a distorted tetrahedral (HBa_4) environment (Fig. 1B). It can be also considered anion-ordered HT-BaH_2 in which half of H1 is replaced by X (see Fig. 1). We found that the "stabilization" of the HT-BaH_2 structure at low temperature by anion ordering makes Ba_2H_3X excellent H^- conductors together with low activation energies (ca. 35 to 50 kJ mol^{-1}). The highest conductivity was achieved for X = I with 1.4×10^{-3} S cm^{-1} at 200°C. This result could open new avenues for hydride-based energy devices and material conversion systems that operate at low temperatures.

RESULTS

Crystal structure and nonstoichiometry

Polycrystalline Ba_2H_3X (X = Cl, Br, and I) samples were prepared by reacting stoichiometric quantities of BaH_2 and BaX_2 at 650°C for 20 hours in an Al_2O_3 tube loaded into an evacuated silica tube. All the powder specimens obtained are white, and their bandgaps were estimated from the diffuse reflectance spectrum to be around 3.1 eV,

[1]Department of Energy and Hydrocarbon Chemistry, Graduate School of Engineering, Kyoto University, Nishikyo-ku, Kyoto 615-8510, Japan. [2]Department of Materials Molecular Science, Institute for Molecular Science, Okazaki, Aichi 444-8585, Japan. [3]SOKENDAI (The Graduate University for Advanced Studies), Okazaki, Aichi 444-8585, Japan. [4]Joining and Welding Research Institute, Osaka University, Ibaraki, Osaka 567-0047, Japan. [5]Institute of Materials Structure Science, High Energy Accelerator Research Organization (KEK), Tokai, Ibaraki 319-1106, Japan. [6]Materials and Life Science Division, J-PARC Center, Tokai, Naka, Ibaraki 319-1195, Japan. [7]Nanostructures Research Laboratory, Japan Fine Ceramics Center, Nagoya, Aichi 456-8587, Japan. [8]CREST, Japan Science and Technology Agency (JST), Kawaguchi, Saitama 332-0012, Japan. [9]Institute for Integrated Cell-Material Sciences (iCeMS), Kyoto University, Sakyo-ku, Kyoto 606-8501, Japan.
*Corresponding author. Email: kage@scl.kyoto-u.ac.jp

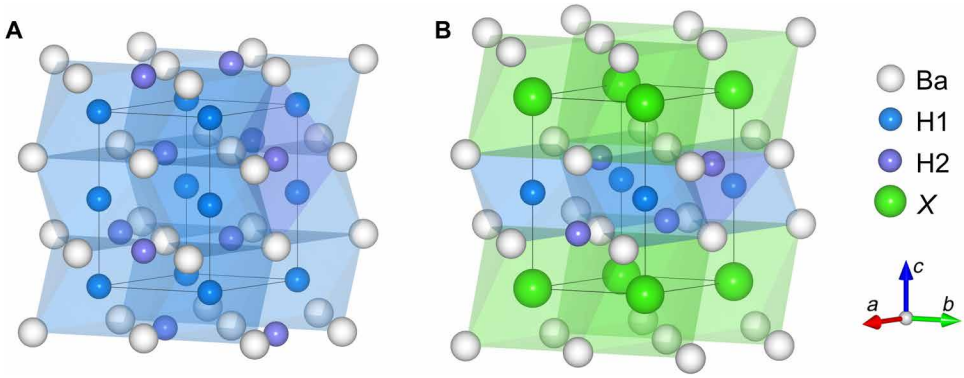

Fig. 1. Structural comparison between BaH_2 and Ba_2H_3X. (**A**) The HT phase of BaH_2 (space group, $P6_3/mmc$), composed of faced-shared hexagonal stacking of $H1Ba_6$ octahedra (anti-NiAs structure), with additional hydride anions at $H2Ba_5$ bipyramidal interstitials (*13*). (**B**) Ordered anion substitution in HT-BaH_2 ("Ba_2H_4") results in Ba_2H_3X (X = Cl, Br, and I; space group, $P\bar{3}m1$), composed of alternate stacking of faced-shared $H1Ba_6$ and XBa_6 octahedra, with hydride anions at $H2Ba_4$ tetrahedral interstitials.

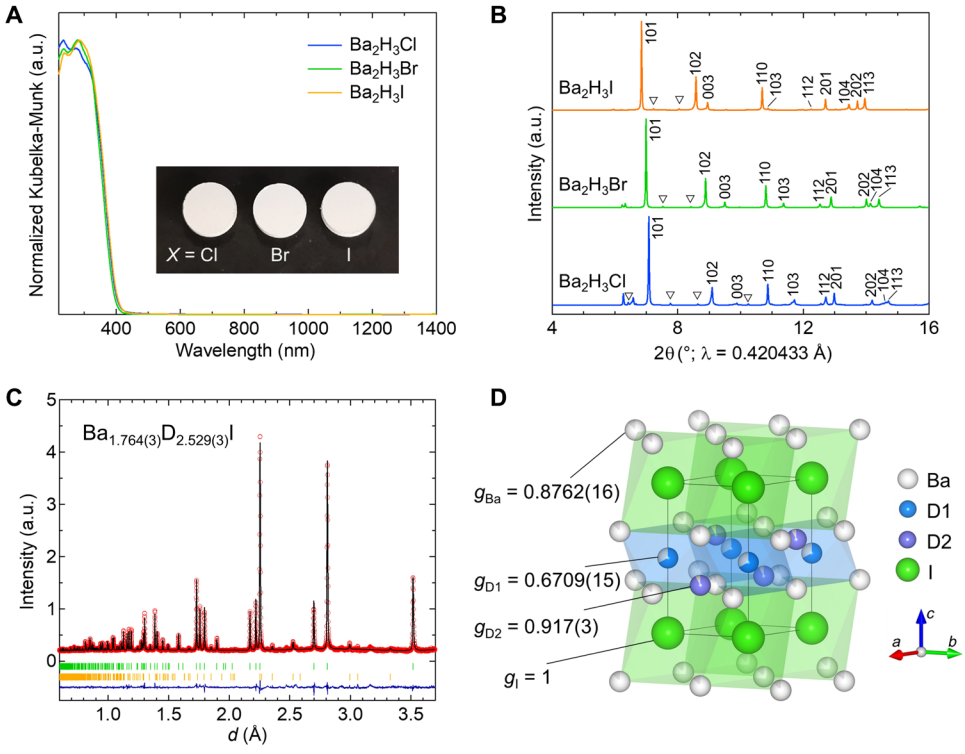

Fig. 2. Characterizations of polycrystalline Ba_2H_3X (X = Cl, Br, and I). (**A**) Ultraviolet-visible diffuse reflectance spectra demonstrating the presence of a wide bandgap. The inset represents a photograph of Ba_2H_3X pellets. (**B**) SXRD patterns of Ba_2H_3Cl (blue), Ba_2H_3Br (green), and Ba_2H_3I (orange), indexed to the space group $P\bar{3}m1$. Triangles denote a small amount (< 5%) of impurity BaHX. (**C**) Rietveld refinement on NPD pattern of deuterated sample of X = I, assuming Schottky defects (Ba^{2+}:D^- = 1:2). Red circles, black line, and blue line represent observed, calculated, difference intensities, respectively. Green and orange ticks indicate Bragg peak positions of $Ba_{1.764(3)}D_{2.529(3)}I$ and BaDI. See details in table S2. (**D**) The refined structure of $Ba_{1.764(3)}D_{2.529(3)}I$, where the occupancy factor g of each site is given. a.u., arbitrary units.

which are in agreement with those from first-principles calculations (Fig. 2A and fig. S2). The synchrotron x-ray diffraction (SXRD) pattern for X = I (Fig. 2B) could be indexed by a hexagonal lattice of a = 4.51276(4) Å and c = 8.0832(10) Å. These values are in reasonable agreement with those of the single crystal Ba_2H_3I [a = 4.5186(12) Å and c = 8.118(2) Å] (*21*), although they are slightly different. The lattice constants for X = Cl and Br are also compatible with the reported values (table S1) (*22*). Note that each SXRD profile contains a minor impurity BaHX (< 5%).

In the previous studies (*21*, *22*), the structure of Ba_2H_3X was determined by single-crystal x-ray diffraction, and the hydrogen positions (1*a* and 2*d*) were only deduced from the analysis of the Madelung potentials and the bond valence sum. We therefore measured neutron powder diffraction (NPD) using the deuterated sample Ba_2D_3I and performed the Rietveld refinement. This readily converged with reasonable reliability factors (R_p = 4.51% and R_{wp} = 6.61%), but with large residual peaks (e.g., 101 at d ~ 3.5 Å), as shown in fig. S3. No improvement in the fit assuming different

crystallographic sites for each atom suggests a nonstoichiometric composition, such as hydride vacancies that generate F-centers. However, given the sample color (white) and the bandgap of 3.1 eV (Fig. 2A), it is unlikely that electrons trapped in impurity levels are present. Furthermore, the absence of sizable defect-induced electrons is supported by the very small and nearly temperature-independent magnetic susceptibility (fig. S4). These results strongly suggest that under our synthetic condition, charge-neutral Schottky defects of Ba^{2+} and $2H^-$ are generated, thus resulting in the composition of $Ba_{2-\delta}H_{3-2\delta}X$.

The inclusion of the Schottky defects in the refinement substantially improved the agreement (R_p = 3.29% and R_{wp} = 4.41%; Fig. 2, C and D, and table S2) and gave $Ba_{1.764(3)}D_{2.529(3)}I$ (δ = 0.236). The occupancy factor of the tetrahedral (H2) site is higher than that of the octahedral (H1) site. Furthermore, the Ba/I ratio of 1.73 estimated by ion chromatography (IC) agrees well with the value from NPD. The refinements for X = Cl and Br with the Schottky defects resulted in $Ba_{1.724(3)}D_{2.447(2)}Cl$ (δ = 0.276) and $Ba_{1.812(4)}D_{2.618(3)}Br$ (δ = 0.188), with the same tendency in the hydride occupancy (figs. S5 and S6 and tables S3 and S4). IC measurements also showed consistent Ba/X ratios of 1.60 (Cl) and 1.64 (Br). The formation of the Schottky defects of Ba^{2+} and $2H^-$ probably causes the discrepancy in the lattice parameters between the single crystals (*21*, *22*) and our powder samples. We found a linear relationship between the Ba/I ratio and the lattice volume in $Ba_{2-\delta}H_{3-2\delta}I$ (fig. S7). However, such lattice variation (or the amount of Schottky defects) does not substantially affect the ionic conductivity, at least within the range examined. It should be noted that the hydride vacancies in $BaH_{2-\delta}$ (δ ~ 0.2) determined from NPD are similar to our compound, although the resulting electrons were assumed to be localized as F-centers (*13*).

To obtain further insight into the Schottky defects, we estimated the formation energies of point defects under hydrogen-rich conditions using first-principles calculations, but the results did not fully explain the experimental observations (fig. S8). For example, in Ba_2H_3I, the formation energies of $V_{H1b}\cdot$ and V_{Ba}'', which are found as major defects, are only 0.2 eV lower than that of H_i'. This implies the presence of H_i to some extent, but hydrogen was not detected at the H_i site within the experimental accuracy by neutron diffraction. In addition, although the binding energy of a V_H and V_{Ba} pair is reasonably high (e.g., 0.37 eV for X = I), the formation energy of associated defect of a pair of $V_H\cdot$ and V_{Ba}' is also high (e.g., 0.69 eV for X = I). Considering the high concentration of Schottky defects observed in $Ba_{2-\delta}H_{3-2\delta}X$, interactions among Schottky defects (clustered Schottky defects) may be taken into account, as reported in TiO_2 (*23*) and UO_2 (*24*). We also point out that some low-energy phonon vibrations of hydride anions are involved in the defect formation, as seen in hydrogen storage alloys (*25*) and Li_3HCh and Na_3HCh (Ch = S, Se, and Te) (*20*).

Hydride conductivity

The ionic conductivities of $Ba_{2-\delta}H_{3-2\delta}X$ (δ ~ 0.2) were measured by electrochemical impedance spectroscopy (EIS) for 20° to 400°C using as-synthesized pellets. Note that there is no noticeable change in the XRD profiles before and after the EIS experiments (figs. S9 and S10 and table S5). Figure 3A displays the representative Cole-Cole plots at 200°C with a semicircle in the high-frequency region and a sharp rise in the low-frequency region, corresponding to the contribution from the bulk/grain boundary and the electrode, respectively

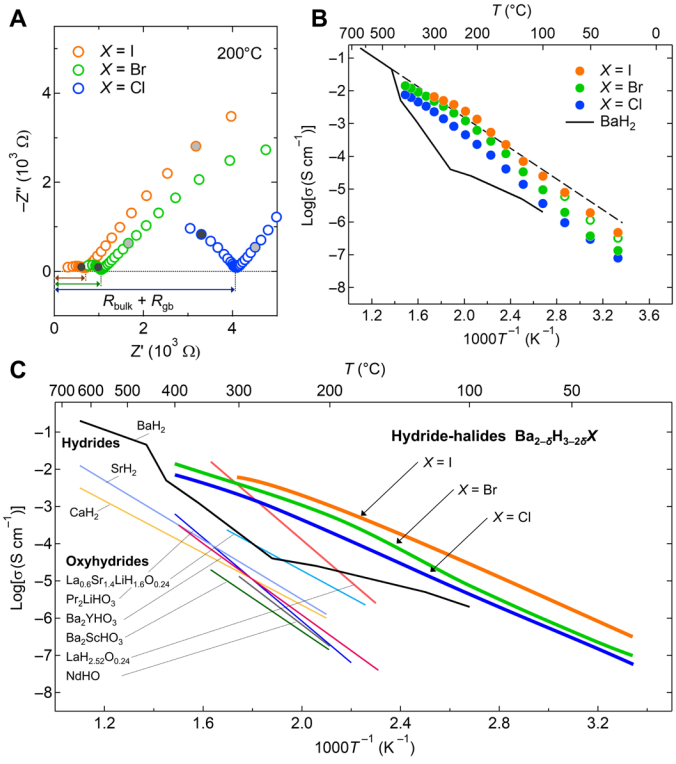

Fig. 3. Hydride conductive properties of $Ba_{2-\delta}H_{3-2\delta}X$ (X = Cl, Br, and I; δ ~ 0.2). (**A**) Impedance plots for $Ba_{2-\delta}H_{3-2\delta}X$ at 200°C. The black and gray filled circles indicate measured frequencies of 10^6 and 10^2 Hz, respectively. (**B**) Arrhenius plots of the total conductivity of $Ba_{2-\delta}H_{3-2\delta}X$. The open green circles represent the bulk conductivity of X = Br, which could be separated from the total conductivity only at low temperatures (≤ 75°C). The dotted black line is an extrapolation of the total conductivity of the HT phase of BaH_2 to low temperatures. (**C**) Thermal evolution of the total conductivity of the hydride-halides $Ba_{2-\delta}H_{3-2\delta}X$, together with those of other hydride conductors (*13*–*17*, *27*). Note that the bulk conductivities are shown for $LaH_{2.52}O_{0.24}$ and NdHO (*18*, *19*).

(details in fig. S11 and table S6). The temperature evolution of total conductivity (σ_{total}) for $Ba_{2-\delta}H_{3-2\delta}X$, calculated from the sum of the bulk and grain boundary resistances, is shown in Fig. 3B. The Hebb-Wagner polarization (*26*) for X = I was measured to identify the charge carriers. We obtained a sufficiently small electronic conductivity $\sigma_{e,h} = 7.98 \times 10^{-6}$ S cm^{-1} at 200°C (fig. S12), indicating that the main contribution to the observed conductivity is ionic, with a transport number of $t_{ion} = (\sigma_{total} - \sigma_{e,h})/\sigma_{total} > 0.99$. The high total conductivity observed in the relatively low temperature region is hardly conceivable for the divalent Ba^{2+} conduction. Negligible halide ion conduction is supported theoretically by the much higher formation energy of $V_X\cdot$ (1.3 eV) compared to that of $V_H\cdot$ (fig. S8) and experimentally by the higher conductivity for the larger X^-, along with a lower concentration (X/H ~ 1/3). Overall, these factors indicate that the H^- ion is the only carrier.

In Fig. 3C, we compare the thermal evolution of total conductivities of $Ba_{2-\delta}H_{3-2\delta}X$ (δ ~ 0.2) with those of the reported H^- conductors (*13*–*19*, *27*). The conductivities in the range of 10^{-3} to 10^{-2} S cm^{-1} above 300°C are comparable to those of known representative materials such as BaH_2 (~5×10^{-3} S cm^{-1} at 420°C) (*13*) and $LaH_{2.52}O_{0.24}$ (2.6×10^{-2} S cm^{-1} at 342°C) (*18*). $Ba_{2-\delta}H_{3-2\delta}X$ exhibit excellent total conductivities below 300°C. Even at 200°C, the total conductivity is

as high as 10^{-4} to 10^{-3} S cm^{-1}. It is also worth noting that the H^- conductivity can be measured down to room temperature in all samples, where a distinct semicircle is consistently observed at high frequencies (fig. S11 and table S6). Clearly, such fast conduction over a lower-temperature range is enabled by the low activation energy (35 to 50 kJ mol^{-1}), in contrast to $LaH_{2.52}O_{0.24}$ with an activation energy of 125 kJ mol^{-1} (*18*).

DISCUSSION

The key to understanding the superior H^- conductivity of $Ba_{2-\delta}H_{3-2\delta}X$ becomes clearer by comparing it with the structurally related BaH_2. As mentioned above, the rapid decrease in the conductivity of BaH_2 at 450°C results from the structural transition from the hexagonal structure (Fig. 1A) to the distorted orthorhombic one (fig. S1) (*13*). Extrapolation of the conductivity of the HT phase of BaH_2 to low temperatures (broken line in Fig. 3B) is roughly in agreement with that of $Ba_{2-\delta}H_{3-2\delta}X$. This observation strongly suggests that the superior conductivity in $Ba_{2-\delta}H_{3-2\delta}X$ is achieved by "stabilizing" the HT-BaH_2 structure through ordered anion substitution with halide anions (Fig. 1), in a stark contrast to the introduction of chemical disorder applied to conventional ionic conductors including YSZ (*1*, *2*). One might be surprised to see the correspondence in conductivity between $Ba_{2-\delta}H_{3-2\delta}X$ and the "hypothetical" HT-BaH_2 (broken line in Fig. 3B), because the latter has a three-dimensional (3D) H^- network and contains ca. 33% more H^- ions. However, this result is coherent with the preferential 2D conduction that is proposed in HT-BaH_2 based on the large anisotropic thermal vibrations of H1 (*13*).

From the crystal structure of $Ba_{2-\delta}H_{3-2\delta}X$, it is evident that the H^- migration occurs within the $Ba_{2-\delta}H_{3-2\delta}$ slab. This was also verified by the climbing image nudged elastic band (CI-NEB) calculations for Ba_2H_3X. Among the possible H^- vacancy hopping routes, the lowest migration energy of 0.22 eV (X = Cl), 0.20 eV (X = Br), and 0.17 eV (X = I) is found for the nearest-neighbor H1–H2 path (Fig. 4, fig. S13, and table S7). Given the relatively lower values compared to the experimental activation energy (0.37 to 0.5 eV), the binding energy of a V_H and V_{Ba} pair must be considered. The sum of the migration energy and the binding energy is 0.63 eV (X = Cl), 0.64 eV (X = Br), and 0.54 eV (X = I), which is higher but comparable to the experimental activation energy. This overestimation is probably due to the effects of phonon vibrations and interactions among multiple point defects as described above. For a more quantitative analysis, these effects need to be taken into account in the calculations. The higher ionic conductivity in the order of X = Cl < Br < I (e.g., 0.23, 0.63, and 1.4 mS cm^{-1} at 200°C) is not simply explained in terms of the size effect, because both H1–H2 distance and bottleneck size for H^- diffusion hardly depend on X species (fig. S14). Important here could be the softness of anions ($Cl^- < Br^- < I^-$) (*28*), as underlined in Li^+ conductors such as LGPS ($Li_{10}GeP_2S_{12}$) and argyrodite (Li_6PS_5X; X = Cl, Br, and I) (*29*–*31*).

Chemical disorder induced by substitution with dopants randomly distributed in the immobile ion sublattice is, apart from morphological control (*32*–*34*), a general strategy to stabilize HT phases at lower temperatures and achieve fast ionic conductivity (*1*–*8*). Such chemical substitution inevitably introduces different parameters at the same time, including changes in local bonding nature and coordination environment (*35*–*38*), that might complicate a thorough understanding of the mechanism of ionic conductivity. In marked contrast, the present study demonstrates the case where an ordered arrangement of anions can maintain the lattice free from or minimized chemical disorder, giving an ideal opportunity to study the intrinsic nature of H^- conductivity. Because many mixed-anion compounds adopt layered anion-ordered structures based on the concept of HSAB (hard and soft acids and bases) and the Hume-Rothery rule (*39*), ordered mixed anionization will lead to a new development in a variety of ion conducting materials, not only in the hydride system.

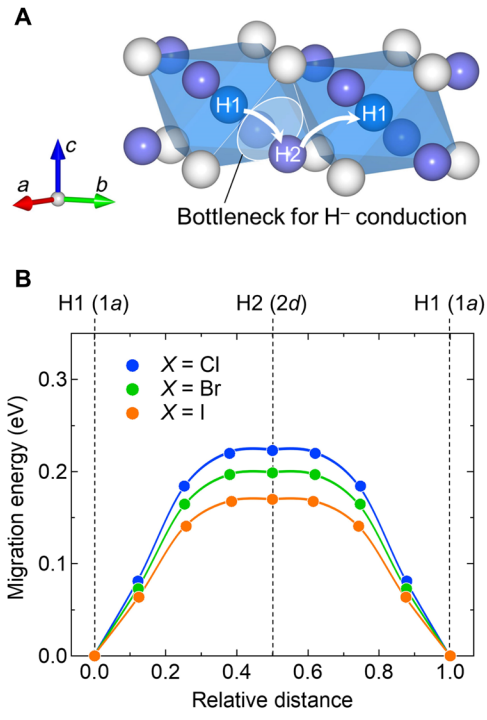

Fig. 4. Proposed hydride conduction in $Ba_{2-\delta}H_{3-2\delta}X$ (X = Cl, Br, and I). (**A**) H^- diffusion pathway via the vacancy mechanism in $Ba_{2-\delta}H_{3-2\delta}$ layer. The white spheres are barium ions. The blue and purple spheres indicate hydride ions at H1 (Wyckoff position 1*a*) and H2 (2*d*) sites, respectively. (**B**) Migration energy from CI-NEB calculation of H1–H2–H1 pathway.

Perspectives

The observation of H^- conduction at low temperatures may give rise to various functions such as catalysis, not limited to ionic conductivity. For example, several oxyhydrides such as $BaTi(O,H)_3$ $BaCe(O,N,H)_{3-\delta}$ have recently been shown as catalytically active in NH_3 synthesis and CO_2 methanation at about 300°C, indicating that the lability of the H^- ions, combined with the strong basicity, is involved in these catalytic activities (*11*, *40*, *41*). An isotope experiment is a facile method to examine the exchangeability of H^- ions in a solid with hydrogen species in the outer atmosphere (*9*, *42*). To see this, the $Ba_{2-\delta}H_{3-2\delta}X$ powder was heated in a D_2 gas stream, and the downstream gas was analyzed by quadrupole mass spectroscopy (see Materials and Methods). Figure 5 shows that H/D exchange started already at 100°C, much lower than for typical oxyhydride compounds [e.g., 350°C for $BaTi(O,H)_3$] (*9*, *42*). Such a low temperature H/D exchange makes $Ba_{2-\delta}H_{3-2\delta}X$ a promising candidate material that could allow various inorganic hydrogenations under milder conditions, with much room for material optimization, e.g.,

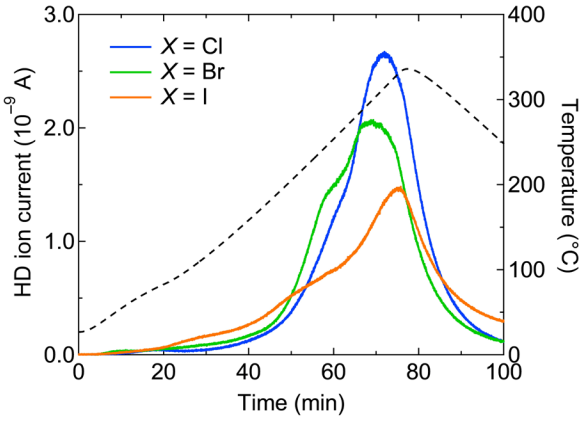

Fig. 5. Mass spectroscopy during isotope exchange for $Ba_{2-\delta}H_{3-2\delta}X$ (X = Cl, Br, and I). Each powder sample of $Ba_{2-\delta}H_{3-2\delta}X$ was heated under a flow of D_2/Ar gas, while ion current of evolved HD gas was monitored. The black dotted line indicates the temperature as a function of time. After this treatment, x-ray diffraction showed no noticeable change in lattice parameters or crystallinity.

by chemical substitution. Furthermore, labile H^- ions at (near) room temperature could even offer a new direction in organic synthesis chemistry. The hydride-halides are stable for several gases and aprotic solvents (fig. S15). The strong reducing property and high nucleophilicity of "free" H^- ions, instead of hydride clusters in conventional reductive reagents such as $LiAlH_4$ and $NaBH_4$, may convert various unsaturated bonds into useful saturated ones by allowing free H^- ions to react directly with hydrocarbons, possibly leading to unexplored reaction routes that are crucial for fine chemical synthesis including pharmaceuticals.

MATERIALS AND METHODS

Synthesis of Ba_2H_3X (X = Cl, Br, and I)

We prepared the powder samples of Ba_2H_3X (X = Cl, Br, and I) using a conventional solid-state reaction. Powders of BaH_2 (Mitsuwa Chemical, 99.5%) and BaX_2 (X = Cl, Ba, and I) (Wako, 99.99%) were thoroughly ground and mixed, and then the mixture was pressed into a pellet (4 to 10 mm in diameter and 1 to 2 mm in thickness). The pellets were loaded into an alumina tube. The tube was then placed in a sealed and evacuated silica tube, followed by heating at 650°C for 20 hours. For neutron diffraction experiments, we prepared deuterated samples of Ba_2D_3X in the same method but using BaD_2. BaD_2 was synthesized by reacting barium metal (Sigma-Aldrich, > 99%) with deuterium gas (Taiyo Nippon Sanso, 99.8%). After Ba chunks were loaded into a SUS (steel use stainless) container, the container was evacuated and filled with deuterium gas, which was repeated five times to remove the residual N_2. The sample was heated at 550°C for 30 min in 0.2 MPa of D_2 gas, with two intermediate grindings. Owing to the air- and moisture-sensitive nature of the reactants and products, all handling was carried out in a nitrogen-filled glovebox. The quality of the sample was determined using a Rigaku SmartLab powder XRD apparatus.

Sample characterizations

High-resolution SXRD experiments were performed at room temperature using a large Debye-Scherrer camera installed at SPring-8 BL02B2 with λ = 0.420344(1) Å. Powder samples were loaded into capillaries (0.5 mm in diameter). During measurements, the capillaries were rotated for better averaging of the powder pattern intensities and removal of possible preferential orientation effects. The obtained SXRD profiles were analyzed by the Le Bail method using the Fullprof program (*43*). Using powder samples of Ba_2D_3X (X = Cl, Br, and I), time-of-flight NPD experiments were carried out at room temperature using a SPICA diffractometer at J-PARC. Approximately 1 g of powder sample was loaded in a vanadium-nickel cell (radius of 6 mm and height of 55 mm). The obtained NPD profiles were analyzed by the Rietveld method using the Z-Rietveld program (*44*).

The ultraviolet-visible spectra were collected using a Shimadzu UV-2600 spectrophotometer. The temperature dependence of magnetic susceptibility was measured by using a Quantum Design MPMS-XL SQUID magnetometer between 5 and 300 K at a constant magnetic field of 1 T. The Ba/X ratio of the sample was estimated by IC using a Thermo Fisher Scientific ICS-1600 for Ba^{2+} and using an ICS-2000 for X^-.

Electrochemical characterizations

Electrochemical measurements were carried out on sintered pellets of Ba_2H_3X (X = Cl, Br, and I) specimens with the relative density of around 80% (4 to 10 mm in diameter and 1 to 2 mm in thickness) using a Bio-Logic MTZ-35 frequency response analyzer. Ionic conductivity was measured by AC impedance methods with an applied frequency of 0.1 Hz to 35 MHz using gold electrodes for both sides in a flow of H_2 gas for 27° to 400°C. The temperature in the measurement container was controlled by a TOYO Corporation HT-Z3-800 furnace control system. The obtained impedance spectra were analyzed using the EC-Lab software. The equivalent circuits used in the analysis were described in the Supplementary Materials. Electrical conductivities were estimated by the Hebb-Wagner polarization method (*26*) using an asymmetric (−)Pd/Ba_2H_3I/Au(+) cell, where Pd electrode was used as a reversible electrode for H_2. The measurement was carried out using a Bio-Logic VSP-300 multichannel potentiostat in a flow of H_2 gas at 200°C, with an applied potential between 0.3 and 1.9 V.

H/D exchange experiment

H/D exchange experiments were performed at heating rate of 5°C min^{-1} over the temperature range of 20° to 350°C under flowing 5% D_2/Ar. The Ba_2H_3X (X = Cl, Br, and I) samples (typically ~30 mg) were placed in an Al crucible. The evolved gas species (m/z = 2 and 3 for H_2 and HD) were recorded as a function of time using the Bruker MS9610 mass spectrometer.

First-principles calculations

First-principles calculations based on the density functional theory were performed to investigate the band structures and the migration energies using the projector augmented-wave method implemented in the Vienna Ab initio Simulation Package (VASP) code (*45*–*48*). The band structures were calculated using the unit cell of Ba_2H_3X (X = Cl, Br, and I) shown in Fig. 1B. The supercell containing 3 × 3 × 2 unit cells was constructed to calculate point defect formation energies (*49*, *50*) of Ba vacancy (V_{Ba}), H vacancy (V_H), X vacancy (V_X), interstitial H (H_i), and interstitial X (X_i). The binding energy (*51*) of a pair of V_H and V_{Ba} was also estimated in Ba_2H_3X. All the symmetrically independent structures including one V_H and one V_{Ba} were calculated. On the basis of the results of the experimental crystal structure

analysis and the calculation of defect formation energies, the migration energies were calculated for the diffusion paths of H1–H1, H1–H2, and H2–H2 sites of H^- ion vacancy with the charge state +1, V_{H^-}. In the calculation models, the vacancy concentration of 1.85% (1/54), corresponding to $\delta \sim 0.04$ in $Ba_{2-\delta}H_{3-2\delta}X$, was used. This concentration is lower than the experimentally obtained value of $\delta \sim 0.2$, but it is known that the migration energy obtained from a model with low defect concentration usually agrees well with the experimental results for samples with high degree of defects (*52*, *53*). The exchange-correlation term was treated with the Heyd-Scuseria-Ernzerhof hybrid functional (HSE06) (*54*) for the calculation of the band structure and Generalized Gradient Approximation and Perdew-Burke-Ernzerhof functional (GGA-PBE) (*55*) for the point defect formation and migration energies. The plane-wave cutoff energy was set to be 520 eV. The integration in the reciprocal space was performed using $6 \times 6 \times 3$ and $2 \times 2 \times 2$ Γ-centered grids for the unit cell and the supercell, respectively. Structure optimization was carried out until that all residual forces acting on each atom become less than 0.02 eV/Å. The migration energies of H^- ion via vacancy mechanisms were calculated using the CI-NEB method with three intermediate images (*56*, *57*).

SUPPLEMENTARY MATERIALS

Supplementary material for this article is available at http://advances.sciencemag.org/cgi/content/full/7/23/eabf7883/DC1

REFERENCES AND NOTES

1. S. Hull, Superionics: Crystal structures and conduction processes. *Rep. Prog. Phys.* **67**, 1233–1314 (2004).
2. V. Thangadurai, W. Weppner, Recent progress in solid oxide and lithium ion conducting electrolytes research. *Ionics* **12**, 81–92 (2006).
3. S. Kim, H. Oguchi, N. Toyama, T. Sato, S. Takagi, T. Otomo, D. Arunkumar, N. Kuwata, J. Kawamura, S.-i. Orimo, A complex hydride lithium superionic conductor for high-energy-density all-solid-state lithium metal batteries. *Nat. Commun.* **10**, 1081 (2019).
4. P. Lacorre, F. Goutenoire, O. Bohnke, R. Retoux, Y. Laligant, Designing fast oxide-ion conductors based on $La_2Mo_2O_9$. *Nature* **404**, 856–858 (2000).
5. S. Adams, R. Prasada Rao, Ion transport and phase transition in $Li_{7-x}La_3(Zr_{2-x}M_x)O_{12}$ ($M = Ta^{5+}$, Nb^{5+}, $x = 0, 0.25$). *J. Mater. Chem.* **22**, 1426–1434 (2012).
6. H. Maekawa, M. Matsuo, H. Takamura, M. Ando, Y. Noda, T. Karahashi, S.-i. Orimo, Halide-stabilized $LiBH_4$, a room-temperature lithium fast-ion conductor. *J. Am. Chem. Soc.* **131**, 894–895 (2009).
7. K. Yoshida, T. Sato, A. Unemoto, M. Matsuo, T. Ikeshoji, T. J. Udovic, S.-i. Orimo, Fast sodium ionic conduction in $Na_2B_{10}H_{10}$-$Na_2B_{12}H_{12}$ pseudo-binary complex hydride and application to a bulk-type all-solid-state battery. *Appl. Phys. Lett.* **110**, 103901 (2017).
8. S. Saha, G. Rousse, M. Courty, Y. Shakhova, M. Kirsanova, F. Fauth, V. Pomjakushin, A. M. Abakumov, J. M. Tarascon, Structural polymorphism in $Na_4Zn(PO_4)_2$ driven by rotational order–disorder transitions and the impact of heterovalent substitutions on na-ion conductivity. *Inorg. Chem.* **59**, 6528–6540 (2020).
9. Y. Kobayashi, O. J. Hernandez, T. Sakaguchi, T. Yajima, T. Roisnel, Y. Tsujimoto, M. Morita, Y. Noda, Y. Mogami, A. Kitada, M. Ohkura, S. Hosokawa, Z. Li, K. Hayashi, Y. Kusano, J. e. Kim, N. Tsuji, A. Fujiwara, Y. Matsushita, K. Yoshimura, K. Takegoshi, M. Inoue, M. Takano, H. Kageyama, An oxyhydride of $BaTiO_3$ exhibiting hydride exchange and electronic conductivity. *Nat. Mater.* **11**, 507–511 (2012).
10. N. Masuda, Y. Kobayashi, O. Hernandez, T. Bataille, S. Paofai, H. Suzuki, C. Ritter, N. Ichijo, Y. Noda, K. Takegoshi, C. Tassel, T. Yamamoto, H. Kageyama, Hydride in $BaTiO_{2.5}H_{0.5}$: A labile ligand in solid state chemistry. *J. Am. Chem. Soc.* **137**, 15315–15321 (2015).
11. Y. Kobayashi, Y. Tang, T. Kageyama, H. Yamashita, N. Masuda, S. Hosokawa, H. Kageyama, Titanium-based hydrides as heterogeneous catalysts for ammonia synthesis. *J. Am. Chem. Soc.* **139**, 18240–18246 (2017).
12. M. Hattori, S. Iijima, T. Nakao, H. Hosono, M. Hara, Solid solution for catalytic ammonia synthesis from nitrogen and hydrogen gases at 50 °C. *Nat. Commun.* **11**, 2001 (2020).
13. M. C. Verbraeken, C. Cheung, E. Suard, J. T. S. Irvine, High H^- ionic conductivity in barium hydride. *Nat. Mater.* **14**, 95–100 (2015).
14. G. Kobayashi, Y. Hinuma, S. Matsuoka, A. Watanabe, M. Iqbal, M. Hirayama, M. Yonemura, T. Kamiyama, I. Tanaka, R. Kanno, Pure H^- conduction in oxyhydrides. *Science* **351**, 1314–1317 (2016).
15. Y. Iwasaki, N. Matsui, K. Suzuki, Y. Hinuma, M. Yonemura, G. Kobayashi, M. Hirayama, I. Tanaka, R. Kanno, Synthesis, crystal structure, and ionic conductivity of hydride ion-conducting Ln_2LiHO_3 (Ln = La, Pr, Nd) oxyhydrides. *J. Mater. Chem. A* **6**, 23457–23463 (2018).
16. F. Takeiri, A. Watanabe, A. Kuwabara, H. Nawaz, N. I. P. Ayu, M. Yonemura, R. Kanno, G. Kobayashi, Ba_2ScHO_3: H^- conductive layered oxyhydride with H^- site selectivity. *Inorg. Chem.* **58**, 4431–4436 (2019).
17. H. Nawaz, F. Takeiri, A. Kuwabara, M. Yonemura, G. Kobayashi, Synthesis and H^- conductivity of a new oxyhydride Ba_2YHO_3 with anion-ordered rock-salt layers. *Chem. Commun.* **56**, 10373–10376 (2020).
18. K. Fukui, S. Iimura, T. Tada, S. Fujitsu, M. Sasase, H. Tamatsukuri, T. Honda, K. Ikeda, T. Otomo, H. Hosono, Characteristic fast H^- ion conduction in oxygen-substituted lanthanum hydride. *Nat. Commun.* **10**, 2578 (2019).
19. H. Ubukata, T. Broux, F. Takeiri, K. Shitara, H. Yamashita, A. Kuwabara, G. Kobayashi, H. Kageyama, Hydride conductivity in an anion-ordered fluorite structure LnHO with an enlarged bottleneck. *Chem. Mater.* **31**, 7360–7366 (2019).
20. S. Gao, T. Broux, S. Fujii, C. Tassel, K. Yamamoto, Y. Xiao, I. Oikawa, H. Takamura, H. Ubukata, Y. Watanabe, K. Fujii, M. Yashima, A. Kuwabara, Y. Uchimoto, H. Kageyama, Hydride-based antiperovskites with soft anionic sublattices as fast alkali ionic conductors. *Nat. Commun.* **12**, 201 (2021).
21. O. Reckeweg, F. J. DiSalvo, Filling up another gap: Synthesis and crystal structure of Ba_2H_3I. *Z. Für Naturforschung B.* **66**, 1087–1091 (2011).
22. O. Reckeweg, J. C. Molstad, S. Levy, F. J. DiSalvo, Syntheses and crystal structures of the new ternary barium halide hydrides Ba_2H_3X (X = Cl or Br). *Z. Für Naturforschung B.* **62**, 23–27 (2007).
23. J. He, S. B. Sinnott, *Ab Initio* calculations of intrinsic defects in rutile TiO_2. *J. Am. Ceram. Soc.* **88**, 737–741 (2005).
24. E. Vathonne, J. Wiktor, M. Freyss, G. Jomard, M. Bertolus, DFT + *U* investigation of charged point defects and clusters in UO_2. *J. Phys. Condens. Matter* **26**, 325501 (2014).
25. N. Otani, A. Kuwabara, T. Ogawa, C. A. J. Fisher, I. Tanaka, E. Akiba, Equilibrium hydrogen pressures in the V–H system from first principles. *Int. J. Hydrogen Energy* **44**, 28909–28918 (2019).
26. B. J. Neudecker, W. Weppner, Li_9SiAlO_8: A lithium ion electrolyte for voltages above 5.4 V. *J. Electrochem. Soc.* **143**, 2198–2203 (1996).
27. M. C. Verbraeken, E. Suard, J. T. S. Irvine, Structural and electrical properties of calcium and strontium hydrides. *J. Mater. Chem.* **19**, 2766–2770 (2009).
28. S. Hati, B. Datta, D. Datta, Polarizability of an ion in a molecule. Applications of Rittner's model to alkali halides and hydrides revisited. *J. Phys. Chem.* **100**, 19808–19811 (1996).
29. N. Kamaya, K. Homma, Y. Yamakawa, M. Hirayama, R. Kanno, M. Yonemura, T. Kamiyama, Y. Kato, S. Hama, K. Kawamoto, A. Mitsui, A lithium superionic conductor. *Nat. Mater.* **10**, 682–686 (2011).
30. Y. Wang, W. D. Richards, S. P. Ong, L. J. Miara, J. C. Kim, Y. Mo, G. Ceder, Design principles for solid-state lithium superionic conductors. *Nat. Mater.* **14**, 1026–1031 (2015).
31. M. A. Kraft, S. P. Culver, M. Calderon, F. Böcher, T. Krauskopf, A. Senyshyn, C. Dietrich, A. Zevalkink, J. Janek, W. G. Zeier, Influence of lattice polarizability on the ionic conductivity in the lithium superionic argyrodites Li_6PS_5X (X = Cl, Br, I). *J. Am. Chem. Soc.* **139**, 10909–10918 (2017).
32. R. Makiura, T. Yonemura, T. Yamada, M. Yamauchi, R. Ikeda, H. Kitagawa, K. Kato, M. Takata, Size-controlled stabilization of the superionic phase to room temperature in polymer-coated AgI nanoparticles. *Nat. Mater.* **8**, 476–480 (2009).
33. M. Tatsumisago, Y. Shinkuma, T. Minami, Stabilization of superionic α-AgI at room temperature in a glass matrix. *Nature* **354**, 217–218 (1991).
34. A. Hayashi, K. Noi, A. Sakuda, M. Tatsumisago, Superionic glass-ceramic electrolytes for room-temperature rechargeable sodium batteries. *Nat. Commun.* **3**, 856 (2012).
35. J. B. Goodenough, Oxide-ion conductors by design. *Nature* **404**, 821–823 (2000).
36. Y. Yamazaki, F. Blanc, Y. Okuyama, L. Buannic, J. C. Lucio-Vega, C. P. Grey, S. M. Haile, Proton trapping in yttrium-doped barium zirconate. *Nat. Mater.* **12**, 647–651 (2013).
37. R. Perriot, B. P. Uberuaga, Structural *vs*. intrinsic carriers: Contrasting effects of cation chemistry and disorder on ionic conductivity in pyrochlores. *J. Mater. Chem. A* **3**, 11554–11565 (2015).
38. N. Minafra, M. A. Kraft, T. Bernges, C. Li, R. Schlem, B. J. Morgan, W. G. Zeier, Local charge inhomogeneity and lithium distribution in the superionic argyrodites Li_6PS_5X (X = Cl, Br, I). *Inorg. Chem.* **59**, 11009–11019 (2020).
39. H. Kageyama, K. Hayashi, K. Maeda, J. P. Attfield, Z. Hiroi, J. M. Rondinelli, K. R. Poeppelmeier, Expanding frontiers in materials chemistry and physics with multiple anions. *Nat. Commun.* **9**, 772 (2018).
40. Y. Tang, Y. Kobayashi, C. Tassel, T. Yamamoto, H. Kageyama, Hydride-enhanced CO_2 methanation: Water-stable $BaTiO_{2.4}H_{0.6}$ as a new support. *Adv. Energy Mater.* **8**, 1800800 (2018).
41. M. Kitano, J. Kujirai, K. Ogasawara, S. Matsuishi, T. Tada, H. Abe, Y. Niwa, H. Hosono, Low-temperature synthesis of perovskite oxynitride-hydrides as ammonia synthesis catalysts. *J. Am. Chem. Soc.* **141**, 20344–20353 (2019).

42. Y. Tang, Y. Kobayashi, K. Shitara, A. Konishi, A. Kuwabara, T. Nakashima, C. Tassel, T. Yamamoto, H. Kageyama, On hydride diffusion in transition metal perovskite oxyhydrides investigated via deuterium exchange. *Chem. Mater.* **29**, 8187–8194 (2017).
43. J. Rodríguez-Carvajal, Recent advances in magnetic structure determination by neutron powder diffraction. *Phys. B Condens. Matter.* **192**, 55–69 (1993).
44. R. Oishi, M. Yonemura, Y. Nishimaki, S. Torii, A. Hoshikawa, T. Ishigaki, T. Morishima, K. Mori, T. Kamiyama, Rietveld analysis software for J-PARC. *Nucl. Instrum. Methods Phys. Res. Sect. Accel. Spectrometers Detect. Assoc. Equip.* **600**, 94–96 (2009).
45. G. Kresse, J. Furthmüller, Efficient iterative schemes for *ab initio* total-energy calculations using a plane-wave basis set. *Phys. Rev. B.* **54**, 11169–11186 (1996).
46. G. Kresse, D. Joubert, From ultrasoft pseudopotentials to the projector augmented-wave method. *Phys. Rev. B.* **59**, 1758–1775 (1999).
47. G. Kresse, J. Hafner, *Ab initio* molecular dynamics for open-shell transition metals. *Phys. Rev. B.* **48**, 13115–13118 (1993).
48. G. Kresse, J. Furthmüller, Efficiency of ab-initio total energy calculations for metals and semiconductors using a plane-wave basis set. *Comput. Mater. Sci.* **6**, 15–50 (1996).
49. Y. Kumagai, F. Oba, Electrostatics-based finite-size corrections for first-principles point defect calculations. *Phys. Rev. B.* **89**, 195205 (2014).
50. C. Freysoldt, J. Neugebauer, C. G. Van de Walle, Fully *Ab Initio* finite-size corrections for charged-defect supercell calculations. *Phys. Rev. Lett.* **102**, 016402 (2009).
51. A. J. E. Rowberg, L. Weston, C. G. Van de Walle, Ion-transport engineering of alkaline-earth hydrides for hydride electrolyte applications. *Chem. Mater.* **30**, 5878–5885 (2018).
52. K. Shitara, A. Kuwabara, K. Hibino, K. Fujii, M. Yashima, J. R. Hester, M. Umeda, N. Nunotani, N. Imanaka, Ionic conduction mechanism in Ca-doped lanthanum oxychloride. *Dalton Trans.* **50**, 151–156 (2021).
53. P. G. Sundell, M. E. Björketun, G. Wahnström, Density-functional calculations of prefactors and activation energies for H diffusion in $BaZrO_3$. *Phys. Rev. B.* **76**, 094301 (2007).
54. A. V. Krukau, O. A. Vydrov, A. F. Izmaylov, G. E. Scuseria, Influence of the exchange screening parameter on the performance of screened hybrid functionals. *J. Chem. Phys.* **125**, 224106 (2006).
55. J. P. Perdew, A. Ruzsinszky, G. I. Csonka, O. A. Vydrov, G. E. Scuseria, L. A. Constantin, X. Zhou, K. Burke, Restoring the density-gradient expansion for exchange in solids and surfaces. *Phys. Rev. Lett.* **100**, 136406 (2008).
56. G. Henkelman, H. Jónsson, Improved tangent estimate in the nudged elastic band method for finding minimum energy paths and saddle points. *J. Chem. Phys.* **113**, 9978–9985 (2000).
57. G. Henkelman, B. P. Uberuaga, H. Jónsson, A climbing image nudged elastic band method for finding saddle points and minimum energy paths. *J. Chem. Phys.* **113**, 9901–9904 (2000).

Acknowledgments

Funding: This work was partly supported by CREST grant nos. JPMJCR1421 and JPMJCR20R2; JSPS KAKENHI grant nos. JP16H06438, JP16H06439, JP16H06440, JP16H06441, and JP19H04710; Nanotechnology Platform Program (Molecule and Material Synthesis) (S-20-MS-0015) from the Ministry of Education, Culture, Sports, Science and Technology (MEXT) of Japan; and Japan Society for the Promotion of Science (JSPS) Core-to-Core Program (JPJSCCA20200004). The SXRD experiments were performed at SPring-8 with the approval of JASRI. The NPD experiment was performed at J-PARC (2019S10). The IC measurements were conducted by Sumika Chemical Analysis Service Ltd. H.U. was supported by JSPS Research Fellowships for Young Scientists. G.K. acknowledges support from JSPS, grant numbers 17H05492 and 20H02828. **Author contributions:** H.K. designed the study. H.U. performed the synthesis, characterizations, and H/D exchange experiments. H.U., C.T., and T.B. performed the structural refinements of the neutron data collected by T.S and T.K. The electrochemical measurements were supervised by G.K. and performed by H.U. and F.T. K.S. and A.K. conducted the DFT calculations. All authors discussed the results. H.U., F.T., and H.K. wrote the manuscript, with contributions from other authors. **Competing interests:** The authors declare that they have no competing financial interests. **Data and materials availability:** All data needed to evaluate the conclusions in the paper are present in the paper and/or the Supplementary Materials.

Submitted 20 November 2020
Accepted 15 April 2021
Published 2 June 2021
10.1126/sciadv.abf7883

Citation: H. Ubukata, F. Takeiri, K. Shitara, C. Tassel, T. Saito, T. Kamiyama, T. Broux, A. Kuwabara, G. Kobayashi, H. Kageyama, Anion ordering enables fast H^- conduction at low temperatures. *Sci. Adv.* **7**, eabf7883 (2021).